

Alma Mater Studiorum Università di Bologna  
Archivio istituzionale della ricerca

Experimentally-validated orthotropic elastic model for Wire-and-Arc Additively Manufactured stainless steel

This is the final peer-reviewed author's accepted manuscript (postprint) of the following publication:

*Published Version:*

Experimentally-validated orthotropic elastic model for Wire-and-Arc Additively Manufactured stainless steel / Laghi V.; Tonelli L.; Palermo M.; Bruggi M.; Sola R.; Ceschini L.; Trombetti T.. - In: ADDITIVE MANUFACTURING. - ISSN 2214-8604. - ELETTRONICO. - 42:(2021), pp. 101999.1-101999.12. [10.1016/j.addma.2021.101999]

*Availability:*

This version is available at: <https://hdl.handle.net/11585/820060> since: 2021-05-11

*Published:*

DOI: <http://doi.org/10.1016/j.addma.2021.101999>

*Terms of use:*

Some rights reserved. The terms and conditions for the reuse of this version of the manuscript are specified in the publishing policy. For all terms of use and more information see the publisher's website.

This item was downloaded from IRIS Università di Bologna (<https://cris.unibo.it/>).  
When citing, please refer to the published version.

(Article begins on next page)

This is the final peer-reviewed accepted manuscript of:

Vittoria Laghi, Lavinia Tonelli, Michele Palermo, Matteo Bruggi, Ramona Sola, Lorella Ceschini, Tomaso Trombetti

Experimentally-validated orthotropic elastic model for Wire-and-Arc Additively Manufactured stainless steel

In: Additive Manufacturing, volume 42, 2021

The final published version is available online at:

<https://doi.org/10.1016/j.addma.2021.101999>

Rights / License:

The terms and conditions for the reuse of this version of the manuscript are specified in the publishing policy. For all terms of use and more information see the publisher's website.

*This item was downloaded from IRIS Università di Bologna (<https://cris.unibo.it/>)*

***When citing, please refer to the published version.***

# Experimentally-validated orthotropic elastic model for Wire-and-Arc Additively Manufactured stainless steel

Vittoria Laghi<sup>1\*</sup>, Lavinia Tonelli<sup>2</sup>, Michele Palermo Ph.D<sup>1</sup>, Matteo Bruggi Ph.D<sup>3</sup>, Ramona Sola Ph.D<sup>2</sup>, Lorella Ceschini Ph.D<sup>1</sup>, Tomaso Trombetti Ph.D<sup>1</sup>

\*corresponding author: [vittoria.laghi2@unibo.it](mailto:vittoria.laghi2@unibo.it)

<sup>1</sup>Department of Civil, Chemical, Environmental and Materials Engineering - University of Bologna, Viale del Risorgimento, 2 – 40136 Bologna, Italy

<sup>2</sup>Department of Industrial Engineering (DIN) - University of Bologna, Viale del Risorgimento, 2 – 40136 Bologna, Italy

<sup>3</sup>Department of Civil and Environmental Engineering - Politecnico di Milano, Piazza Leonardo da Vinci, 32 – 20133 Milano, Italy

## Abstract

Wire-and-Arc Additively Manufactured (WAAM) alloys are characterized by specific mechanical properties which can largely differ from the conventionally-manufactured alloys. In detail, the printing process results in a peculiar microstructure, characterized by preferential crystallographic orientation with respect to the printing direction, leading to an anisotropic mechanical behavior of the printed part.

Previous experimental tests on WAAM-produced stainless steel plates showed in particular a strong anisotropic elastic behavior.

Based on the above, the present work formulates a specific anisotropic elastic model for a WAAM-processed austenitic stainless steel, considering an orthogonally anisotropic (or orthotropic) constitutive law, and a procedure to calibrate the elastic parameters based on the experimental results. In detail, the procedure is applied to calibrate the numerical values of the elastic parameters of a specific WAAM 304L austenitic stainless.

For this aim, specific investigations on both the mechanical and microstructural features were carried out. Experimental tensile tests were performed on specimens with different orientations with respect to the printing direction. In detail, Young's modulus and Poisson's ratios were evaluated for samples oriented along three different orientations with respect to the printing deposition layers: longitudinally (L), transversally (T) and diagonally (D) to them. Digital Image Correlation (DIC) optical measuring system was used to acquire the full strain fields during the test. Microstructural analysis was also carried out to study the inherent microstructure, characterized by a distinctive grain growth direction,

1 and to assess the preferred crystallographic orientations of specimens extracted along the three  
2 considered directions.

3 The experimental results are used to calibrate the orthotropic elastic model. From the calibrated model  
4 additional material properties in terms of Young's and shear modulus for any printing direction are  
5 derived. The resulting values exhibit very large variations with the printing angle, with ratios between  
6 minimum to maximum values around 2 for the Young's modulus and 3.5 for the shear modulus. This  
7 marked orthotropic behavior could open unexplored design possibilities based on deformability  
8 issues. Additionally, the calibrated orthotropic model can also be used for future experimental  
9 explorations of the mechanical properties of WAAM alloys and for stiffness-based structural design  
10 optimizations.

## 11 **Key words**

13 Wire-and-arc; Stainless steel; Elastic model; Elastic properties; Orthotropic material; Microstructure.

## 1. Introduction

In recent years, the advancement in metal 3D printing technologies has led to various applications in mechanical, aerospace and civil engineering fields. Although the growing interest and variety of use, a proper characterization of the mechanical behavior of the printed metals is still needed.

Among different metal-based additive manufacturing (AM) processes, Wire-and-Arc Additive Manufacturing (WAAM) allows to realize large-scale elements still maintaining freedom in shape and relatively high printing speed rate [1–3].

In the last few years, various research studies focused on the microstructural and mechanical features of WAAM steel evidencing an anisotropic behavior caused by the manufacturing process.

AM processes, indeed, result in a peculiar microstructure, often dominated by large columnar grains, formed by epitaxy, directed along the maximum thermal gradient [4]. As a result, microstructural features, such as preferential crystal orientation due to epitaxy, can affect the extent and the orientation-dependence of mechanical properties of AM parts [5]. Concerning WAAM processes, several research studies evidenced the preferential crystallographic orientation for different directions with respect to the printing layers [6–11]. Such evolution of the crystallographic orientation differently affects the mechanical properties of the printed alloys, depending on the adopted process parameters and feedstock material.

The anisotropic mechanical behavior of WAAM-produced parts has been recently investigated on different alloys. Rafieazad et al. [10] studied low-carbon low-alloy steel in terms of microstructural analysis and tensile strength, along two different directions with respect to the deposition layers (either parallel to the layers, also referred to as longitudinal, or perpendicular to the layers, also referred to as transversal). Ghaffari et al. [12] investigated the whole stress-strain behavior of low-carbon low-alloy steel produced with WAAM, which showed lower elongation at rupture for specimens oriented transversally. Similar results were also presented by Moore et al. [13] on steel specimens. In detail, the specimens oriented perpendicularly to the deposition layers (transversally) showed lower performances both in terms of hardness, strengths and elongations. Other studies focused on the mechanical behavior of high strength steels in terms of different strain evolution and tensile strength of specimens taken along the longitudinal and transversal directions [14,15].

As far as stainless steel is concerned, Ji et al. [16] presented microstructural and mechanical features of 304L steel specimens taken along the two aforementioned directions. Gordon et al. [6] also reported, for the same alloy, the Young's modulus values for both directions, suggesting an anisotropic elastic behavior of WAAM-produced stainless steel specimens. Very recently, Kyvelou et al. [17] presented the results of a microstructural and mechanical characterization of WAAM

1 stainless steel along three different directions, longitudinal (parallel), transversal (perpendicular) and  
2 diagonal at  $45^\circ$  with respect to the deposition layers. From them, a marked anisotropic behavior in  
3 terms of both stiffness and strength has been registered, confirming the need for a proper  
4 characterization of the anisotropic mechanical behavior of WAAM stainless steel, and for the  
5 assessment of the mutual relationships between process, microstructure and mechanical properties.  
6 Since 2017, researchers at University of Bologna carried out mechanical, geometrical and  
7 microstructural analyses on WAAM-produced 304L stainless steel elements [18–22]. The first  
8 investigations on the structural response of the printed outcomes were focused on tensile and  
9 compressive tests on planar and tubular elements, respectively [19]. Then, the attention was devoted  
10 on the material properties, through a detailed microstructural analysis and tensile tests to derive the  
11 key material properties [20] and the influence of the intrinsic geometrical variability in the mechanical  
12 response [22]. From them, a first assessment of partial factors and design values of the main  
13 mechanical parameters for structural engineering purposes was carried out accounting for the  
14 orientation relative to the printing direction [21].

15 The results evidenced different mechanical responses of specimens taken at three different directions  
16 (longitudinal, transversal and diagonal at  $45^\circ$ ) with respect to the printing deposition layers. As far as  
17 tensile strength is concerned, all specimens registered values of yielding and ultimate strengths higher  
18 than the traditionally-manufactured stainless steel, with the largest values registered for those taken  
19 diagonally. Young's modulus values for longitudinal and transversal specimens resulted lower than  
20 the reference value commonly adopted for stainless steel in structural engineering field (200 GPa).  
21 On the other hand, diagonal specimens registered higher values of Young's modulus than the  
22 reference one. Reasoning of this was found in the material microstructure. Indeed, the grain growth  
23 resulted to be perpendicular to the deposition layers, thus highly affecting the mechanical behavior  
24 of the specimens differently oriented [20].

25 Even though the available literature work clearly evidences the anisotropic nature of WAAM alloys,  
26 there is still lack of proper studies specifically focused on the definition of a specific elastic  
27 constitutive material model accounting for this aspect. Indeed, the anisotropic nature of a material  
28 could be conveniently used to obtain higher-performance structures from the same feedstock through  
29 ad-hoc engineering of the printing parameters and printing strategies. For instance, periodic patterns  
30 and optimization of the printing direction are among the possible solutions to efficiently engineer the  
31 printed material.

32 The present work focuses on the formulation of a specific anisotropic elastic model for WAAM  
33 stainless steel, considering an orthogonally anisotropic (or orthotropic) constitutive law, and on a

1 procedure to calibrate the elastic parameters based on the experimental results. In detail, the procedure  
2 is applied to calibrate the numerical values of the elastic parameters of WAAM 304L stainless steel  
3 based on previous experimental results obtained for the specific WAAM process investigated by the  
4 authors.  
5 For this aim, first the results of the mechanical characterization for specimens oriented along different  
6 directions and detailed investigation on the orientation of the microscopic crystal structure are  
7 presented in Sections 2 and 3. Then, Section 4 presents the formulation of the orthotropic elastic  
8 model for WAAM material and the calibration of its parameters. Final considerations are drawn in  
9 the discussion section (Section 5).  
10

## 2. Experimental characterization of WAAM elastic parameters

### 2.1 Mechanical tests

The mechanical properties of WAAM 308LSi stainless steel were investigated through tensile tests carried out at the Structural Engineering and Topography Labs at University of Bologna. The tests were in particular devoted to quantify the influence of the orientation with respect to the printing layers of dog-bone specimens cut from plates, as well as the possible influence of the geometrical irregularities proper of the layer-by-layer WAAM process. Part of these experimental results (as reported in [19–22]) has been considered to calibrate the elastic material model (Sections 3,4).

The specimens were cut from plates realized by MX3D [23] with Gas Metal Arc Welding (GMAW) process using pulse welding arc transfer and starting from an ER308LSi feeding wire. The adopted printing strategy, referred to as “continuous” printing, consists in a layer-upon-layer deposition. The plates were realized with single-layer thickness (nominal thickness of 4 mm). A fixed set of process parameters was adopted, lying within the ranges as shown in Table 1. No arc correction was used during the printing process. The substrate was a printing plate of 1000 x 1000 x 30 mm, with H-type beams welded as support. As evidenced in a previous work [20], the process resulted in plates with chemical composition consistent to AISI 304L.

Table 1: Process parameters for WAAM deposition (Courtesy of MX3D [23]).

Process parameters	Details	Values*
Deposition power	Current	100 - 140 A
	Arc voltage	18 - 21 V
Speed	Welding speed	15 - 30 mm/s
	Wire feed rate	4 - 8 m/min
	Deposition rate	0.5 - 2 kg/h
Distance and angle	Layer height	0.5 - 2 mm
	Electrode to layer angle	90°
Wire	Wire grade	ER308LSi
	Wire diameter	1 mm
Shield gas	Shield gas type	98% Ar, 2%CO <sub>2</sub>
	Shield gas flow rate	10-20 L/min

\*values are provided within typical ranges. For more specific information the interested readers may refer to MX3D [23].



The tensile tests were carried out on a Universal testing machine of 500 kN load capacity. The tests were performed in displacement control, with a loading rate of 2 MPa/s (according to [24]). All tests were monitored through a deformometer of 50-mm gauge length and Digital Image Correlation (DIC) optical measurement (Figure 1).

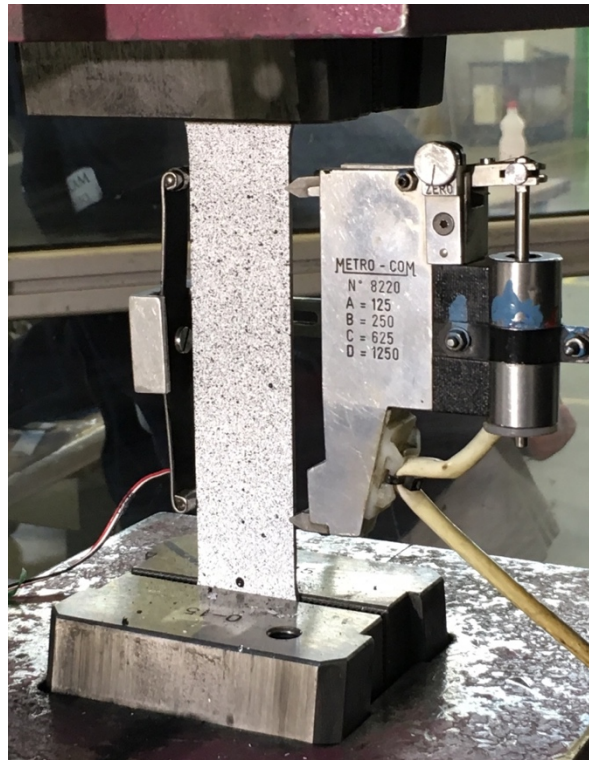


*Figure 1: Tensile test set-up.*

The DIC system was in particular employed to provide highly accurate measurements of the surface strain field along the entire gauge length. The use of DIC is particularly important for WAAM material since the strain field under macroscopic uniaxial loading is not as uniform as for conventionally produced material, as also reported in [17,22]. The outputs of the DIC were processed using Vic3D software to obtain both the longitudinal (i.e. along the longitudinal direction of the specimen) and transversal (i.e. along the transversal direction of the specimen) surface strain fields (punctual values). From the two strain fields, longitudinal and transversal average deformations were evaluated by means of virtual extensometers (see Figures 3 and 4).

In this work, only a subset of the whole experimental results (related to specimens coming from the same batch of plates) is used to calibrate the suitable elastic model of the material. The samples were cut from 4 plates of dimensions 380 x 380 x 4 mm. In particular, for each plate, 3 different specimens

at different orientations with respect to the deposition layers were extracted: parallel to the deposition layers (longitudinal direction, L), perpendicular to the deposition layers (transversal direction, T) and at 45° from them (diagonal direction, D) (Figure 2). The specimens were shaped according to ISO 6892-1 [25] and polished before testing by means of mechanical milling. As a result, the final average thickness was reduced from the initial nominal 4-mm value to 2.5-3 mm. Given the possible influence of the plate thickness in the overall mechanical response (see e.g. [26,27]), the present study refers to results for single-layer thick planar elements.

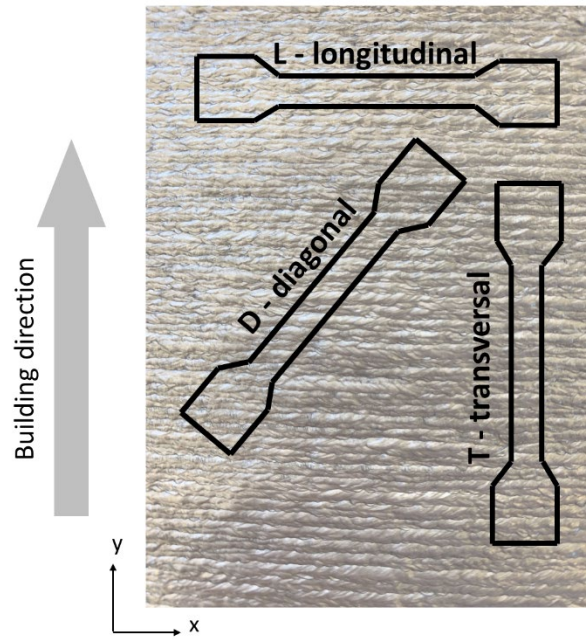


*Figure 2: Schematic representation of the specimens extracted from the printed plates along the three directions L, T and D.*

## 2.2 Microstructural analysis

Microstructural analyses were carried out on samples extracted from grip regions of longitudinal, transversal and diagonal tensile specimens. All three main sections were analysed (xz, xy, zy planes as described in Figure 2). Samples followed a complete metallographic preparation up to polishing to a mirror finish, as described in [28], then were chemically etched by immersion in the Vilella's reagent at room temperature for 20 s (1 g picric acid, 5 mL hydrochloric acid, and 100 mL ethanol [29]). Microstructural characterization at low magnification was performed by means of an Hirox KH7700 3D digital microscope while for the observation at higher magnification a Zeiss Axio Imager A1 optical microscope was adopted.

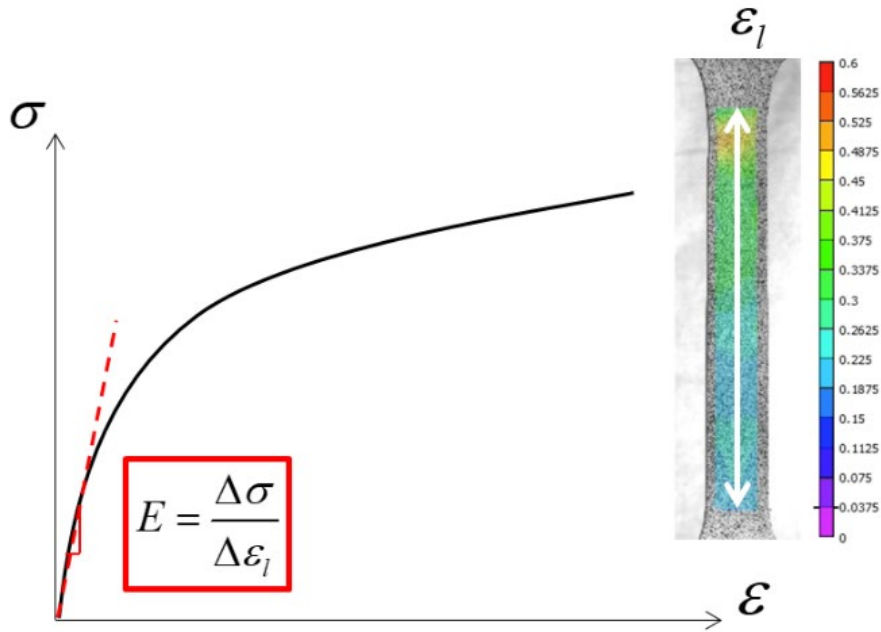
X-Ray diffraction (XRD: X'Pert PRO diffractometer, PANalytical, Almelo, NL) was used to determine phase composition of T, L and D representative samples. Spectra were acquired with a Ni-

1 filtered Cu-K $\alpha$  radiation source in the range  $40^\circ < 2\theta < 100^\circ$ , with a step size of  $0.02^\circ$  and 120 s/step  
2 dwell time, using a 1D array of solid-state detector (X'Celerator PANalytical). Acquired spectra  
3 were elaborated with HighScorePlus software (PANalytical) for phase identification and peaks  
4 characterization, texture coefficients were then obtained following the procedure described by  
5 [30,31].  
6 The same samples were also employed for electron backscatter diffraction (EBSD) analysis. The  
7 latter was carried out using the Nova NanoSEM 450 device, which was equipped with a QC-200 i  
8 (Bruker) EBSD system featuring an e-Flash1000 detector. Samples, placed at an inclination of  $70^\circ$   
9 with respect to the electron beam axis, were scanned at 15 kV acceleration voltage under low-vacuum  
10 (40 Pa) conditions in order to avoid charging drift of their non-conductive surfaces.

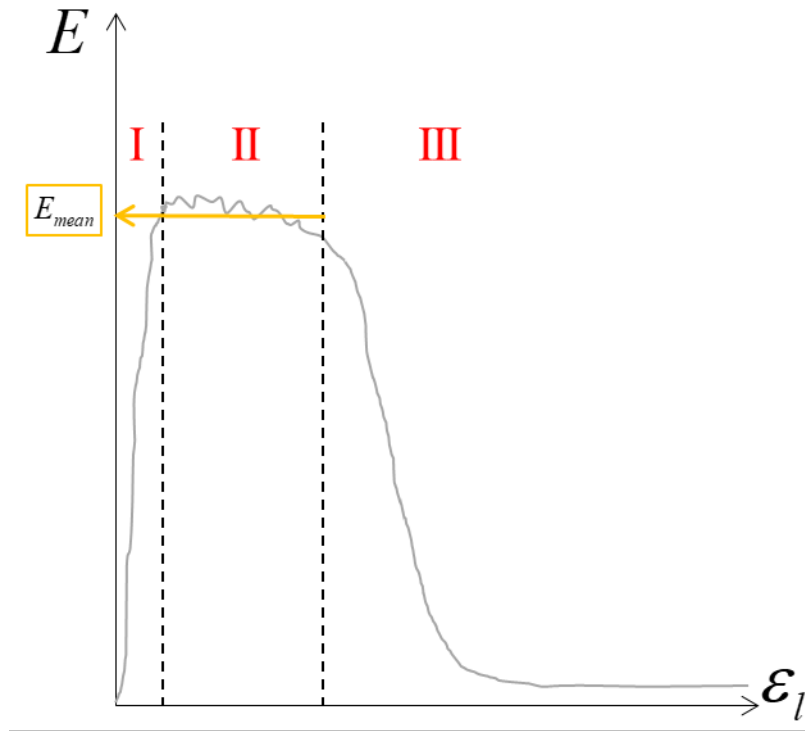
### 3. Results from the experimental characterization

#### 3.1 Elastic parameters from DIC measures

The elastic parameters of WAAM-produced stainless steel were evaluated from the results of the monotonic tensile tests on the machined dog-bone shaped specimens, as described in Section 2.1. For each specimen, the values of Young's modulus  $E$  and Poisson's ratios  $\nu$  were determined from the DIC measures on the average longitudinal  $\varepsilon_l$  (i.e. along the longitudinal direction of the dog-bone specimen) and transversal  $\varepsilon_t$  (i.e. along the transversal direction of the dog-bone specimen) strains. The values of the tangent Young's modulus were calculated from the stress-strain curves obtained from DIC measures on the longitudinal strains  $\varepsilon_l$  (Figure 3a) according to the method recently proposed by Kyvelou et al. [17]. Figure 3b provides a schematic representation of the tangent Young's modulus vs. longitudinal strain  $\varepsilon_l$ . In order to erase any possible experimental noise, the procedure consists in the identification of three regions (Figure 3b): (i) region I is characterized by the initial noise, (ii) region II is characterized by a pseudo-horizontal plateau, and (iii) region III is characterized by decreasing values of the tangent Young's modulus  $E$  with increasing values of  $\varepsilon_l$ . An ordinary least squares regression (OLSR) is then performed to identify the average  $E$  value considering only the values of region II. The procedure was applied on T, L and D specimens.



(a)



(b)

Figure 3: Conceptual schematization of the estimation of the tangent Young's modulus: (a) stress-strain curve, (b) E-strain curve.

The values of Poisson's ratio were estimated as ratios between average transversal and longitudinal strains  $\nu = \frac{\varepsilon_t}{\varepsilon_l}$  at selected cross-sections of L and T specimens (Figure 4a). In particular, in order to consider a possible uneven distribution of the transversal strains along the length of the specimen, the values of  $\varepsilon_t$  were taken as a mean over three measures taken at three different cross-sections, as presented in Figure 4a.

In particular, for specimens L (i.e. oriented parallel to the printing layers), the Poisson's ratio is computed as:

$$\nu_{TL} = \frac{\varepsilon_{t,T}}{\varepsilon_{l,L}} \quad (1)$$

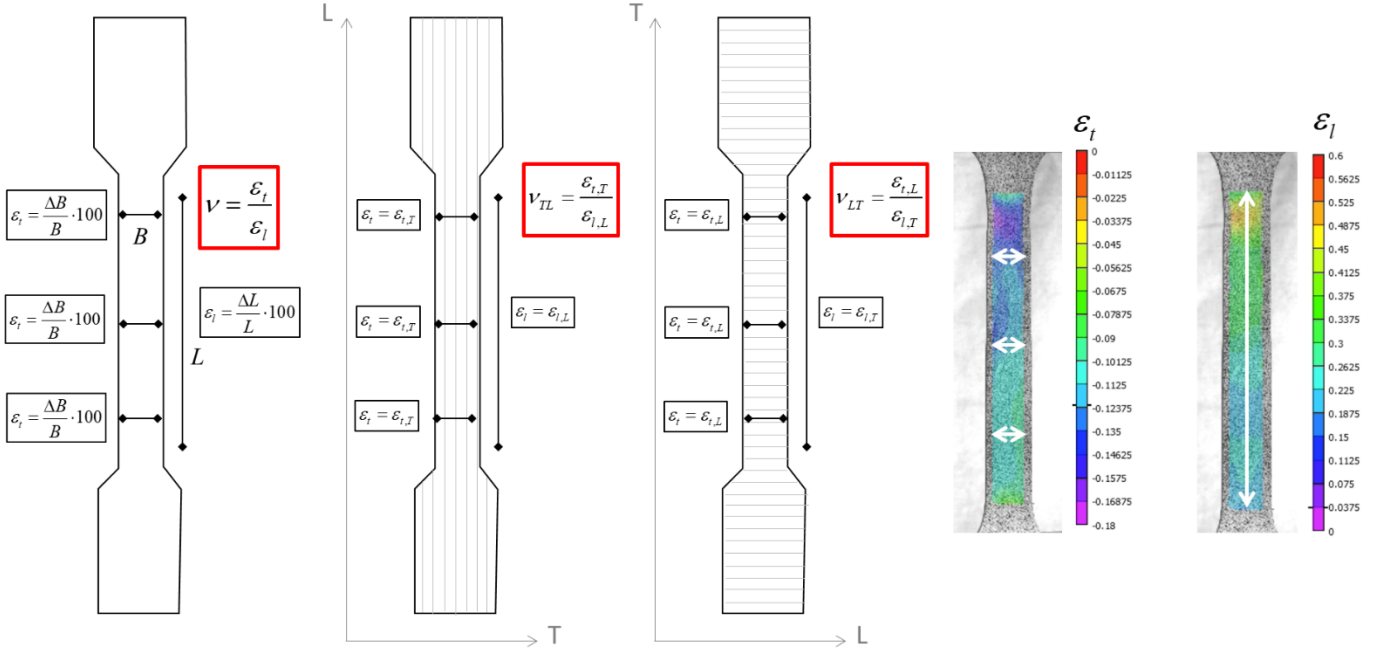
where  $\varepsilon_{t,T}$  refers to the transversal strain estimated along the direction T (i.e. perpendicular to the printing layers), while  $\varepsilon_{l,L}$  refers to the longitudinal strain estimated along the direction L (i.e. parallel to the printing layers).

Likewise, for specimens T (i.e. oriented perpendicular to the printing layers), the Poisson's ratio is computed as:

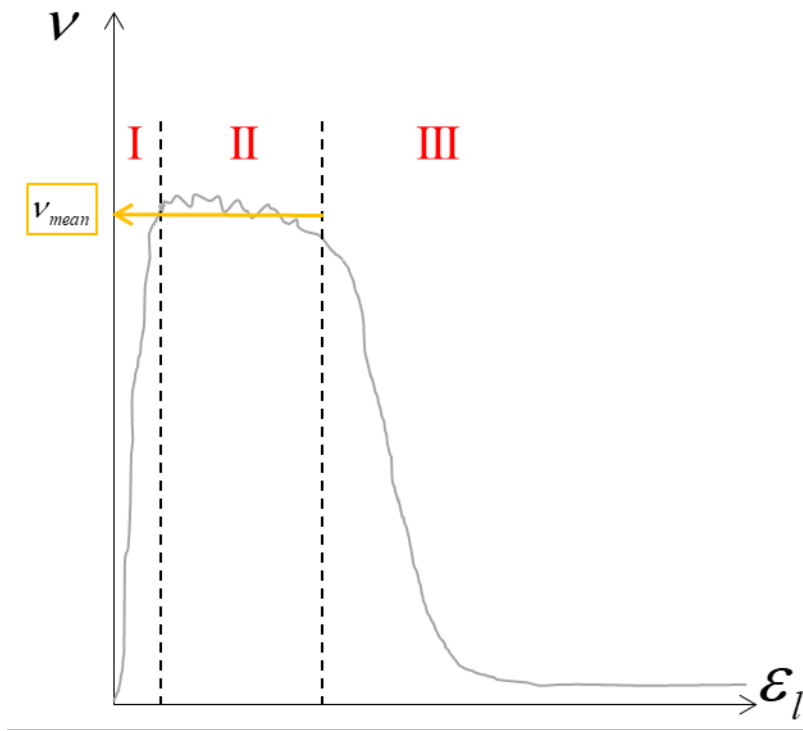
$$\nu_{LT} = \frac{\varepsilon_{t,L}}{\varepsilon_{l,T}} \quad (2)$$

where  $\varepsilon_{t,L}$  refers to the transversal strain estimated along the direction L, while  $\varepsilon_{l,T}$  refers to the longitudinal strain estimated along the direction T.

The method adopted to estimate the tangent Young's modulus was adopted also for the Poisson's ratio, through the definition of the region II of the  $\nu$ - $\varepsilon_l$  curve (Figure 4b).



(a)



(b)

Figure 4: Conceptual schematization of the estimation of the Poisson's ratio: (a) stress-strain curve, (b)  $\nu$ -strain curve.

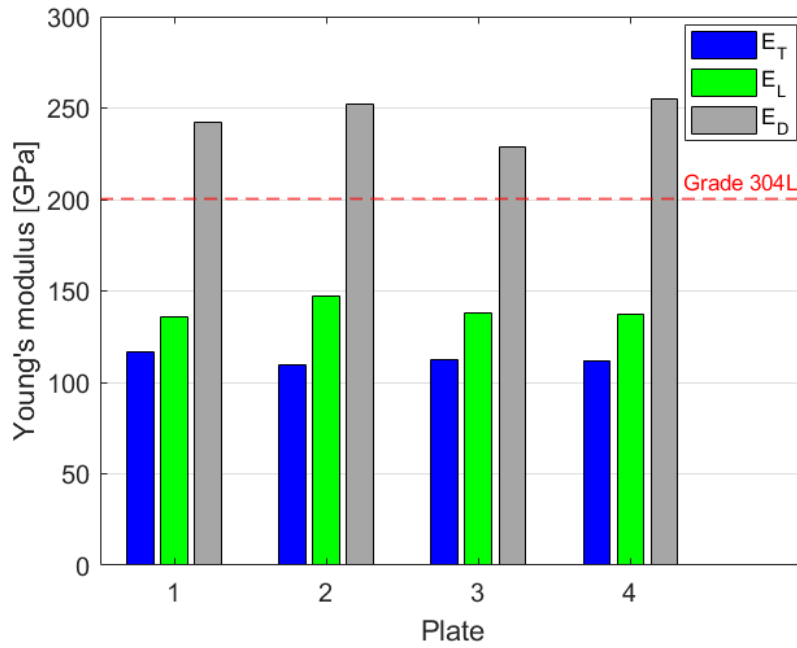
Table 2 collects the values of the elastic parameters (e.g. Young's modulus and Poisson's ratios) for the specimens oriented along the three directions (T, L, D). On average, the different values of Young's modulus along the three directions confirm a marked anisotropy, as well described also in previous research [17,19,20,32]. Moreover, Poisson's ratio values seem to be also affected by the different orientations of the specimens with respect to the printing deposition. Indeed, for T specimens (having the longitudinal axis perpendicular to the deposition layers),  $\nu$  values ( $\nu_{LT}$ ) are considerably lower than those ( $\nu_{TL}$ ) of L specimens.

Table 2: WAAM elastic parameters from tensile tests.

	E [GPa]			$\nu$ [-]	
Plate	T	L	D	LT	TL
1	116.45	135.54	242.06	0.352	0.384
2	109.64	147.31	252.09	0.354	0.494
3	112.27	137.94	228.54	0.356	0.457
4	111.99	137.27	255.31	0.374	0.434

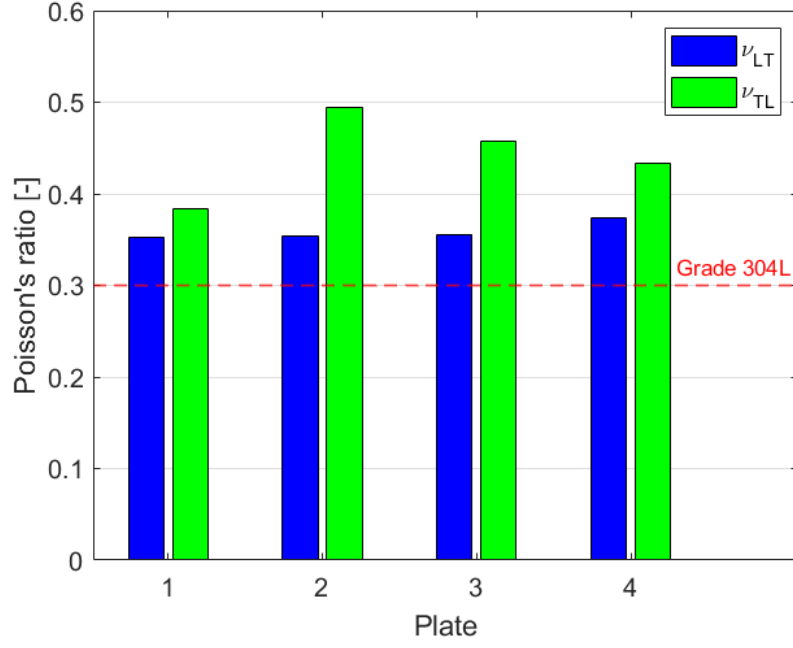
<b>mean</b>	<b>112.59</b>	<b>139.52</b>	<b>244.50</b>	<b>0.359</b>	<b>0.442</b>
<b>COV</b>	<b>0.02</b>	<b>0.03</b>	<b>0.04</b>	<b>0.02</b>	<b>0.09</b>

Figure 5 provides the histograms of the elastic parameters of WAAM stainless steel along the different orientation as compared with those of a traditionally-manufactured stainless steel ( $E=200$  GPa and  $\nu=0.3$  according to ASM Handbook [33]). As far as Young's modulus is concerned (Figure 5a), the trend for the three directions is the same for all four plates. In detail, the lowest values are registered for T specimens, while D specimens have almost 25% higher values than the one commonly adopted for 304L steel. Similar trend is registered for the Poisson's ratio (Figure 5b), for which both specimens T and L provided results 15% to 50% higher than the traditional reference (0.30).



(a)





(b)

Figure 5: Histograms of (a) Young's modulus and (b) Poisson's ratio values for WAAM stainless steel.

It is of interest to compare the values of the products of the Young's modulus along one direction with the Poisson's ratio evaluated for the orthogonal direction, namely  $E_L \cdot \nu_{LT}$  and  $E_T \cdot \nu_{TL}$ . The values are plotted in Figure 6. It can be noted that  $E_L \cdot \nu_{LT} \approx E_T \cdot \nu_{TL}$ .

The symmetry condition  $E_L \cdot \nu_{LT} = E_T \cdot \nu_{TL}$  is a clear indication of an orthotropic material behavior, see e.g. [34].

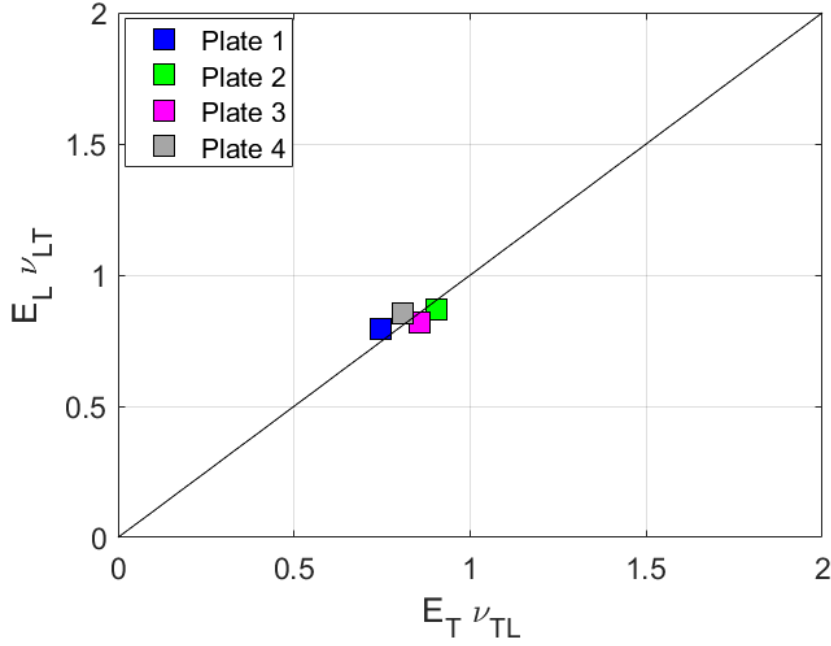


Figure 6: Comparison of Young's moduli and Poisson's ratios along  $T$  and  $L$  directions.

### 3.2 Microstructural features

The microstructure of WAAM samples is shown in Figure 7 where 3D reconstructions obtained by low magnification analyses along  $xy$ ,  $xz$  and  $zy$  planes are reported for the  $T$ ,  $L$  and  $D$  directions. From the micrographs in Figure 7, two peculiar features of additively manufactured parts can be recognized: (i) the layered macro-structure due to the subsequent depositions of molten material, and (ii) the epitaxial grains that have grown over the layers and whose direction is perpendicular to the deposition layer. In fact, due to the peculiar in-process solidification conditions, epitaxial growth occurs and grains grow following the crystallographic orientation of the previously solidified layer [4], possibly leading to crystallographic texture. In Figure 7, layer boundaries and columnar grains are highlighted with yellow and red dashed lines, respectively. In the same figure, also the longitudinal direction of the specimen (coincident with the direction of the applied tensile load) is reported, so it can be clearly seen that layers and grains are differently oriented among  $T$ ,  $L$ , and  $D$  samples with respect to the direction of the applied tensile load. 3D reconstructions also evidenced that cross-sectional area of tensile specimens ( $xz$  plane), in terms of grains and layer boundaries orientation, varies from one direction to another. These aspects were discussed in a previous paper [20] and can justify the different mechanical behavior, in terms of yield and ultimate tensile strength. However, further analyses were needed in order to explain the marked anisotropy of the Young's modulus, clearly related to the crystallographic fibering of specimens. Details of the layer boundary

region, for the three directions, are reported in Figure 8 where two different grain morphologies can be recognized: a fine columnar structure in correspondence of the solidification of a newly deposited layer and a coarser one, where also secondary dendrites can be seen, at the bottom of the boundary due to heating of the previous layer, as also reported by [35]. In the same figure, it can also be seen that growth of the aforementioned columnar grains did not stop at the boundaries, but proceeded across them without changing direction. This phenomenon is likely related to the epitaxial growth that may occur during the rapid solidification experienced by each deposited layer during AM process, where grains grow following the crystallographic orientation of the previously solidified layer [4].

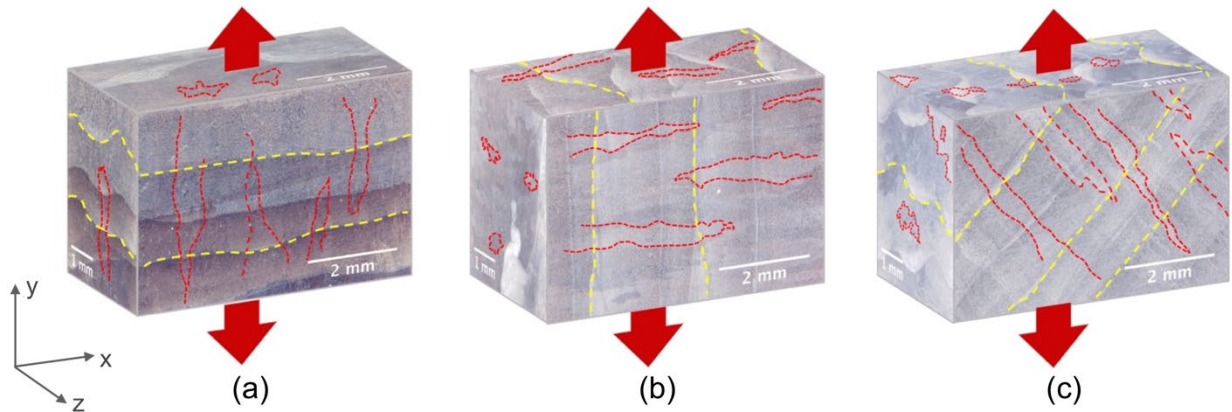


Figure 7: 3D reconstruction of low magnification optical micrographs of tensile specimens: a) transversal, b) longitudinal and c) diagonal specimen. Yellow dashed lines underline the deposited layers while the red ones highlight grain growth; red arrows indicate the loading direction during tests.

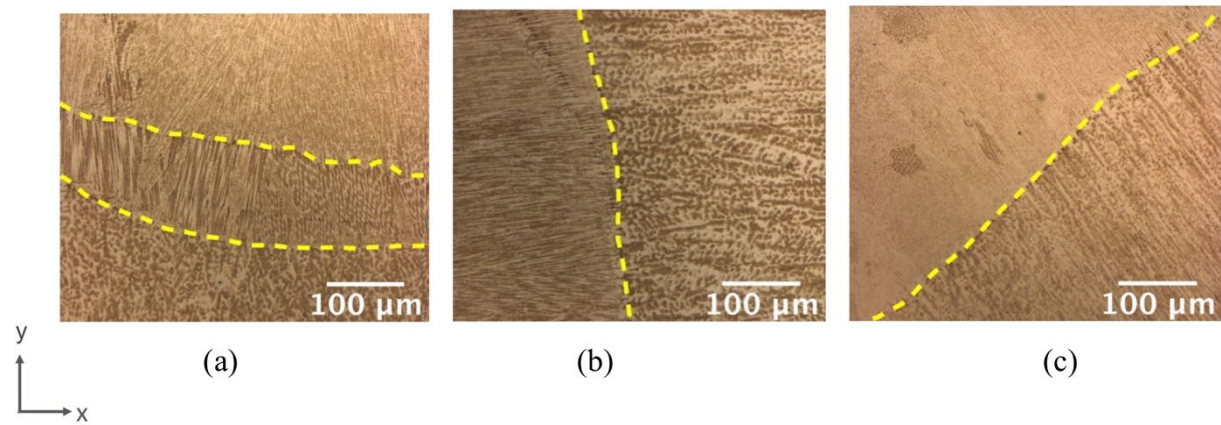


Figure 8: Optical micrographs showing sub-structure within epitaxial grains crossing over layers for: a) transversal, b) longitudinal and c) diagonal specimen. Layer boundaries are highlighted by yellow color.

If this assumption is confirmed, WAAM plates may have developed (during the printing process) a preferential crystallographic orientation of grains and, as a consequence, tensile specimens extracted along T, L and D direction may exhibit different preferential orientations.

In view of the above, the crystal structure was analyzed with XRD, whose results are reported in Figure 9 for a set of representative samples. XRD spectra (Figure 9a) showed that, for all samples, the predominant phase was austenite ( $\gamma$ ), with minor traces of delta-ferrite ( $\delta$ ).

The reference pattern for austenite (ICDD 33-0379) shows five peaks corresponding to (111), (200), (220), (311), (222) crystallographic planes. However, as can be noticed by XRD results, none of the spectra exhibited the (222) austenite peak located at approximately  $95.96^\circ$  and, more importantly, samples showed different peaks characterized also by different peak intensities, suggesting the occurrence of a varied preferred orientation. Specifically, T, L and D directions showed two, four and three austenite peaks respectively.

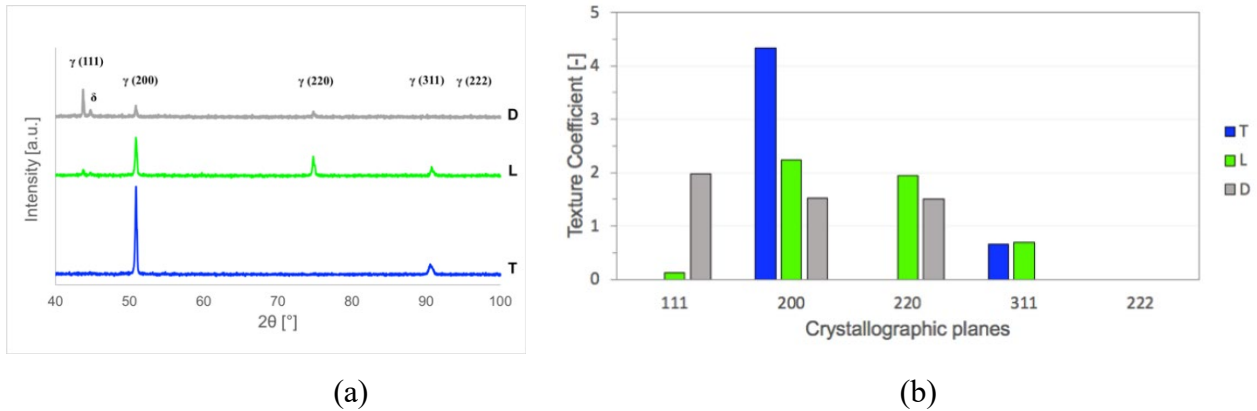


Figure 9: Results of XRD analyses: a) XRD spectra showing phase composition for transversal (T), longitudinal (L) and diagonal (D) specimens; b) texture coefficients for  $\gamma$ -austenite phase derived from spectra

With the aim of quantifying such preferred crystallographic orientations, texture coefficients (TC) for the dominant  $\gamma$ -austenite phase were calculated. The results are reported in Figure 9b. If no preferred orientation exists, TC is equal to 1 for all crystallographic planes, while in case that one or more orientations prevail, TC assumes value higher than 1 for the dominant orientations. Data reported in Figure 9b show that T direction is dominated by (200) orientation, while for L directions (200) and (220) are more predominant. It should be noticed that (111) peak was not revealed on T sample and

was almost negligible for L one, while it prevails on D direction. From the results of the analysis of texture coefficients it can be inferred that a relationship between the Young's modulus obtained with tensile tests and the preferred crystallographic orientation among samples exists. In particular, the dominant orientation of the stiffest direction (D) differs consistently from both L and T ones, which showed instead a much lower Young's modulus. It is well known, indeed, that the fcc-cubic crystal structure of stainless steels is anisotropic and its elastic modulus varies in the range of 101-297 GPa on the basis of the crystal direction, being  $\langle 111 \rangle$  the stiffest direction and  $\langle 100 \rangle$  the least stiff one [36], as also confirmed by experimental characterizations of lattice elastic constants for the AISI 304L stainless steels [37,38]. For the conventional polycrystalline material, with no preferred orientation, the average value of 190-200 GPa is commonly adopted. However, XRD results proved that WAAM plates studied in the present work are characterized by a strong crystallographic texture that can justify the change in the elastic properties according to samples extraction direction.

The presence of a marked crystallographic preferential orientation in the  $\gamma$ -austenite phase was also confirmed by EBSD analyses. According to the inverse pole figures (IPF) and maps reported in Figure 10 for sample D, a texture oriented along the  $\langle 111 \rangle$  crystallographic direction exists. This outcome further supports the above discussion, relating the highest stiffness exhibited by D direction with the stiffest crystallographic direction of the fcc stainless steel lattice structure.

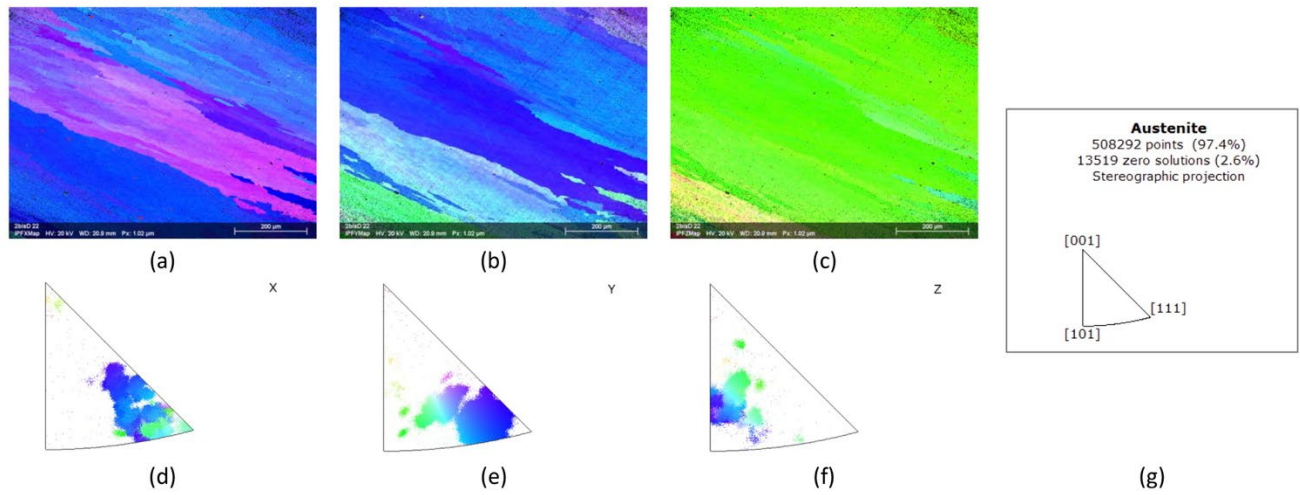


Figure 10: Inverse pole figures (IPF) from EBSD analyses on plane xy for a representative D sample: a) IPFx map; b) IPFy map; c) IPFz map; d), e), f) relative IPF; g) IPF key legend

## 4. Orthotropic material model for WAAM stainless steel

### 4.1 The elastic constitutive model of orthotropic materials

In nature, several materials present different mechanical properties based on their directions in space, and thus are considered as anisotropic. From these, different categories are formed based on the presence of material symmetrical axes or planes.

One example is for the class of orthotropic materials, characterized by two material symmetrical planes orthogonal to each other. Typical orthotropic materials are wood, fiber-reinforced composites with orthogonal pattern, as well as aligned fiber composites. Indeed, any WAAM lamina may be regarded as an aligned layer composite.

The principal axes of these materials are the intersections between the planes of symmetry. For 3D orthotropic materials, the independent elastic constants of the compliance matrix are 9, as identified by three elastic moduli ( $E_x$ ,  $E_y$ ,  $E_z$ ), three independent Poisson's ratios ( $\nu_{xy}$ ,  $\nu_{yz}$ ,  $\nu_{zx}$ ) and three shear moduli ( $G_{xy}$ ,  $G_{yz}$ ,  $G_{zx}$ ).

For the case of a layered lamina undergoing a plane stress state in the plane  $x,y$ , the constitutive equations in the inverse form reduces to [39]:

$$\begin{Bmatrix} \varepsilon_x \\ \varepsilon_y \\ \gamma_{xy} \end{Bmatrix} = \begin{bmatrix} 1/E_x & -\nu_{xy}/E_y & 0 \\ -\nu_{yx}/E_x & 1/E_y & 0 \\ 0 & 0 & 1/G_{xy} \end{bmatrix} \begin{Bmatrix} \sigma_x \\ \sigma_y \\ \tau_{xy} \end{Bmatrix} \quad (3)$$

Thus, the material constitutive law is expressed in terms of only 5 elastic constants, namely  $E_x$ ,  $E_y$ ,  $\nu_{xy}$ ,  $\nu_{yz}$ ,  $G_{xy}$ . Nonetheless, the major symmetries of the elastic tensor call for the symmetry of the compliance matrix, i.e.:

$$E_x \cdot \nu_{xy} = E_y \cdot \nu_{yx} \quad (4)$$

Hence, the number of independent elastic constants reduces to 4.

### 4.2 Calibration of the elastic model for WAAM orthotropic stainless steel

Due to the layered structure of WAAM plates, the two main directions of the orthotropic material  $x$  and  $y$  are selected, reasonably, coincident with the directions L and T, going parallel and perpendicular to the printing deposition layers, respectively (Figure 11). Therefore, in the calibration

process WAAM stainless steel will be assumed to behave as an orthotropic material with the axes of symmetry  $x$  and  $y$  coincident with directions L and T. As already remarked in Section 3 (see Figure 6), the experimental data are also consistent with the symmetry condition expressed by Eq. 4.

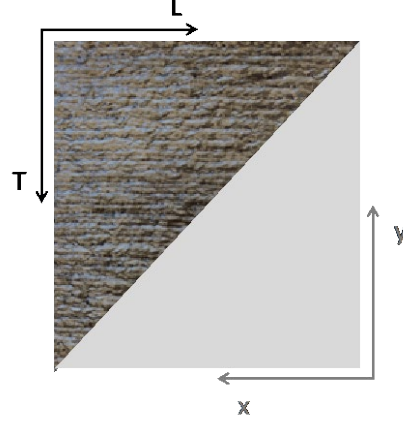


Figure 11: The two directions considered for the real material ( $L$  and  $T$ ) vs. the axes of symmetry ( $x$  and  $y$ ) of an orthotropic model.

From Eq.3, the compliance matrix  $C$  for WAAM stainless steel is:

$$C = \begin{bmatrix} 1/E_x & -\nu_{xy}/E_y & 0 \\ -\nu_{yx}/E_x & 1/E_y & 0 \\ 0 & 0 & 1/G_{xy} \end{bmatrix} \quad (5)$$

In Eq.5,  $E_x$  and  $E_y$  are the Young's moduli along  $x$  and  $y$ , respectively,  $\nu_{xy}$ , and  $\nu_{yx}$  the Poisson's ratios, and  $G_{xy}$  the shear modulus. The Young's moduli  $E_x$  and  $E_y$  are assumed to be coincident to the values obtained from the experimental tests on the four plates (as presented in Section 3.1) along  $L$  and  $T$ , respectively, so that:  $E_x = E_L$  and  $E_y = E_T$ . Additionally, given the experimental values for Young's modulus along direction  $D$ , it is also assumed that the value of the Young's modulus found through transformation of the compliance matrix at an angle  $\alpha = 45^\circ$  corresponds to  $E_D$ .

On the contrary, the values of the Poisson's ratios cannot be, rigorously speaking, simply taken equal to those obtained from the experimental results, but should instead be calibrated to achieve the (full) symmetry of the compliance matrix. Therefore, the following minimization problem can be used to calibrate the values of Poisson's ratios  $\nu_{xy}$ ,  $\nu_{yx}$ , ensuring to satisfy Eq. 4:

$$\begin{cases} \min_{\nu_{xy}, \nu_{yx}} & (\nu_{xy} - \nu_{LT})^2 + (\nu_{yx} - \nu_{TL})^2 \\ s.t. & \nu_{yx} \cdot E_y = \nu_{xy} \cdot E_x \end{cases} \quad (6)$$

with  $\nu_{xy}$  and  $\nu_{yx}$  unknowns. From Eq. 6  $\nu_{xy}$  and  $\nu_{yx}$  can be expressed as follows:

$$\begin{cases} \nu_{xy} = \frac{E_x}{E_x + E_y} \cdot (\nu_{LT} + \nu_{TL}) \\ \nu_{yx} = \frac{E_y}{E_x + E_y} \cdot (\nu_{LT} + \nu_{TL}) \end{cases} \quad (7)$$

From the value of the Young's modulus measured along the diagonal direction  $E_D$  (Table 2), the shear modulus  $G_{xy}$  can be found through transformation of the compliance matrix for  $\alpha = 45^\circ$  (see e.g. [40]) with the following formula:

$$G_{xy} = \left( \frac{4}{E_D} - \frac{1 - \nu_{xy}}{E_x} - \frac{1 - \nu_{yx}}{E_y} \right)^{-1} \quad (8)$$

Table 3 collects the values of the elastic parameters of the orthotropic model for WAAM stainless steel calibrated from the experimental results (as presented in Section 3.1) on the four plates making use of Eqs. 7 and 8.

Table 3: Elastic parameters of the orthotropic model for WAAM stainless steel.

Plate	$E_x$ [GPa]	$E_y$ [GPa]	$G_{xy}$ [GPa]	$\nu_{yx}$ [-]	$\nu_{xy}$ [-]
1	135.54	116.45	156.34	0.396	0.339
2	147.31	109.64	152.47	0.486	0.362
3	137.94	112.27	127.52	0.448	0.365
4	137.27	111.99	168.48	0.445	0.363
<b>mean</b>	<b>139.52</b>	<b>112.59</b>	<b>151.20</b>	<b>0.444</b>	<b>0.357</b>
<b>COV</b>	<b>0.03</b>	<b>0.02</b>	<b>0.10</b>	<b>0.07</b>	<b>0.03</b>



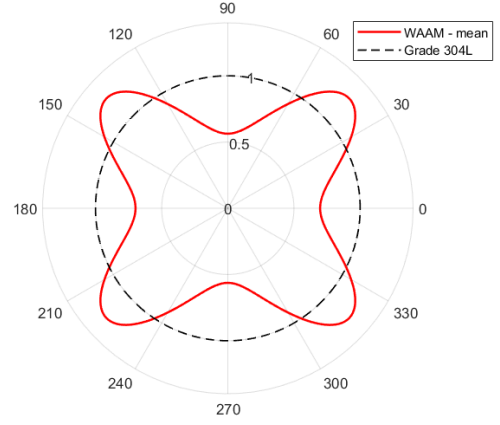
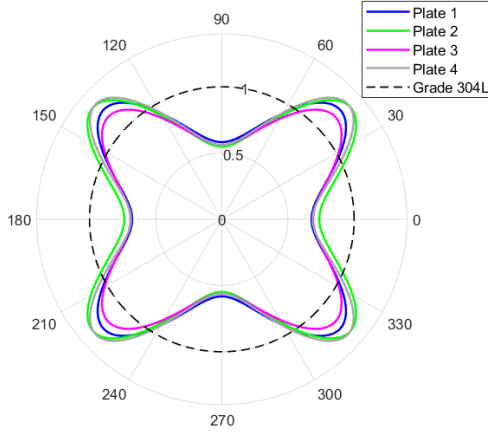
It is of interest to notice that the values of the shear modulus are, on average equal to 150 GPa, which is twice the value commonly adopted for 304L steel (around 77 GPa assuming a Young's modulus equal to 200 GPa and a Poisson's ratio equal to 0.3).

Table 4 collects the discrepancies from experimental and calibrated Poisson's ratios. The values evidence a good agreement between the experimental measures and the calibrated values for almost all plates, for which a difference of around  $\pm 3\%$  is registered. This result is a further confirmation of the orthotropic nature of WAAM stainless steel plates.

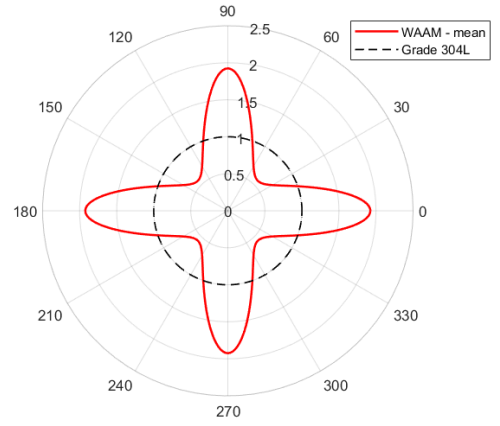
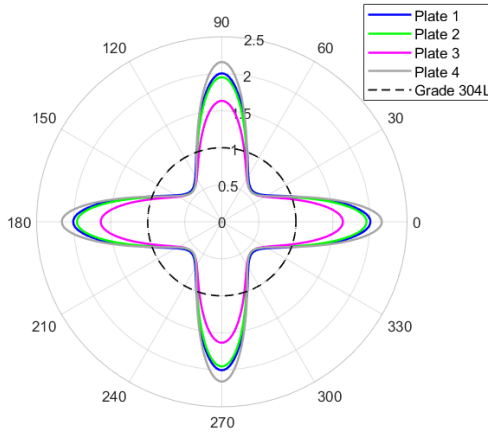
*Table 4: Discrepancy of experimental and calibrated Poisson's ratios.*

Plate	$(\nu_{yx}-\nu_{TL})/\nu_{TL}$ [%]	$(\nu_{xy}-\nu_{LT})/\nu_{LT}$ [%]
1	+3.1%	-3.4%
2	-1.6%	+2.2%
3	-1.9%	+2.4%
4	+2.6%	-3.1%

Figure 12 shows the normalized polar diagrams of the Young's modulus and shear modulus, as computed through transformation of the compliance matrix of Eq. 5, see e.g. [34]. The diagrams are normalized with respect to the standard Young's modulus and shear modulus values for 304L stainless steel (i.e. 200 GPa and 77 GPa, respectively) according to ASM Handbook [33]. The orientation  $\alpha$  is measured from  $x$  (i.e.  $\alpha = 0^\circ$  corresponds to L direction on the real printed material, while  $\alpha = 90^\circ$  corresponds to T direction on the real printed material).



(a)



(b)

Figure 12: Normalized polar diagrams: (a) Young's modulus and (b) shear modulus of WAAM-produced stainless steel and of Grade 304 stainless steel depending on the orientation of the reference system with respect to  $x$ .

Tables 5 and 6 collect the maximum and minimum values and the corresponding orientations  $\alpha$  of Young's modulus and shear modulus calibrated from the values of the four plates tested (Section 3.1).

Table 5: Maximum and minimum values of Young's modulus and corresponding orientations for the four plates tested.

Plate	$E_{\max}$ [GPa]	$\alpha_{E,\max}$ [°]		$E_{\min}$ [GPa]	$\alpha_{E,\min}$ [°]	
1	243.44	$\pm 43^\circ$	$\pm 137^\circ$	116.45	$\pm 90^\circ$	$\pm 270^\circ$
2	257.61	$\pm 41^\circ$	$\pm 139^\circ$	109.64	$\pm 90^\circ$	$\pm 270^\circ$

3	230.98	$\pm 42^\circ$	$\pm 138^\circ$	112.27	$\pm 90^\circ$	$\pm 270^\circ$
4	257.95	$\pm 42^\circ$	$\pm 138^\circ$	111.99	$\pm 90^\circ$	$\pm 270^\circ$
<b>mean</b>	<b>247.50</b>	<b><math>\pm 42^\circ</math></b>	<b><math>\pm 138^\circ</math></b>	<b>112.59</b>	<b><math>\pm 90^\circ</math></b>	<b><math>\pm 270^\circ</math></b>

Table 6: Maximum and minimum values of shear modulus and corresponding orientations for the four plates tested.

Plate	$G_{\max}$ [GPa]	$\alpha_{G,\max}$ [°]		$G_{\min}$ [GPa]	$\alpha_{G,\min}$ [°]	
1	156.44	$\pm 0^\circ$	$\pm 180^\circ$	45.88	$\pm 45^\circ$	$\pm 135^\circ$
2	152.46	$\pm 0^\circ$	$\pm 180^\circ$	44.42	$\pm 45^\circ$	$\pm 135^\circ$
3	127.48	$\pm 0^\circ$	$\pm 180^\circ$	44.14	$\pm 45^\circ$	$\pm 135^\circ$
4	168.46	$\pm 0^\circ$	$\pm 180^\circ$	44.06	$\pm 45^\circ$	$\pm 135^\circ$
<b>mean</b>	<b>151.21</b>	<b><math>\pm 0^\circ</math></b>	<b><math>\pm 180^\circ</math></b>	<b>44.63</b>	<b><math>\pm 45^\circ</math></b>	<b><math>\pm 135^\circ</math></b>

## 5. Discussion and future research

Inspections of the graphs reported in Figure 12 and of Tables 5 and 6 allow to draw interesting observations.

Concerning the Young's modulus (Figure 12a), the minimum values, as expected, are for  $\alpha = \pm 90^\circ$  and  $\pm 180^\circ$ , along the  $x$  coordinate of the material model, or else along the T direction of the real printed plate. On the other hand, the maximum values are not found exactly at  $\pm 45^\circ$  and  $\pm 135^\circ$ , as might be expected from the experimental tests, but instead for  $\alpha$  values on average around  $\pm 42^\circ$ , and  $\pm 138^\circ$ . Reasonings to this are related to the slightly different values of Young's modulus found along the two principal directions of WAAM stainless steel, i.e. longitudinal L (on average of 140 GPa) and transversal T (on average of around 110 GPa). Thus, the orthotropic elastic model calibrated from experiments gives a maximum value which is not exactly at  $45^\circ$  (as would be expected if the values of Young's modulus were equal along both T and L), but instead  $42^\circ$ . Examples of other anisotropic materials with similar behavior were studied in [41].

Comparing the average results obtained on WAAM stainless steel with the traditionally-manufactured 304L steel, the former one presents in general lower values of Young's modulus, especially for  $\alpha = \pm 90^\circ$  and  $\pm 180^\circ$ , while it presents higher values than the traditional stainless steel for angles between  $\pm 25^\circ$  and  $\pm 60^\circ$  (and respectively  $\pm 120^\circ$  and  $\pm 155^\circ$ ). The ratio between maximum and minimum values of  $E$  for WAAM stainless steel is of around 2.

As far as shear modulus diagrams are concerned (Figure 12b), maximum values are registered for  $\alpha = \pm 90^\circ$  and  $\pm 180^\circ$ , with values on average twice the one commonly adopted for 304L steel. Minimum values are, instead, quite below (almost halved) the standard value considered for 304L steel, at  $\alpha = \pm 45^\circ$  and  $\alpha = \pm 135^\circ$ . In general, WAAM stainless steel presents higher values than the traditional stainless steel for angles between  $\pm 70^\circ$  and  $\pm 110^\circ$  (and respectively  $\pm 160^\circ$  and  $\pm 200^\circ$ ), while it is 50% higher for angles between  $\pm 80^\circ$  and  $\pm 100^\circ$  (and respectively  $\pm 170^\circ$  and  $\pm 190^\circ$ ). The ratio between maximum and minimum values of  $G$  for WAAM stainless steel is of around 3.5.

The above outcomes, concerning both Young's and shear moduli, point out a quite marked orthotropy suggesting further experimental investigations to verify these theoretical predictions and to explore the material behavior at different orientations with respect to those already tested. For instance, additional axial tests at different orientations are needed to verify the model prediction, both in terms of Young's modulus and relevant Poisson's ratios. This means measuring the axial elongation and evaluating a transverse contraction coefficient in each test. Directions for which maximum values of the elastic modulus are predicted should be experimentally assessed. Results of off-axis tension tests

can be processed as well to provide an exact determination of the shear modulus, instead of resorting to more complex tests on tubes and plates (see e.g. [42]).

The presented results, enriched with further experimental investigations, will then allow to draw a full experimentally-validated orthotropic material model for WAAM stainless steel, including both the elastic and post-elastic behavior.

Moreover, the calibration of an orthotropic model for WAAM stainless steel also allows to draw unexplored design possibilities in structural design. In details, new design strategies could be explored through the exploitation of the different structural response by changing the printing directions. Possible topology optimization tools could be driven by deformation constraints which can be accurately matched at specific printing orientations [43]. In general, high structural performances could be reached using the same feedstock, if the crystallographic orientation is well engineered, i.e. if the printing directions are set in order to follow the stress paths arising under a prescribed load. For example, considering the simple truss system of Figure 13, an efficient solution to reduce the deformability can be achieved by setting the printing direction of each truss element so that its longitudinal axis is aligned with the orientation of maximum axial stiffness. Also, periodic patterns could be printed to enhance the overall structural performance while saving material.

Finally, advanced materials could also be engineered to realize optimized WAAM-produced structures, through ad-hoc correlation studies on the influence of the printing parameters on the mechanical orthotropic response.

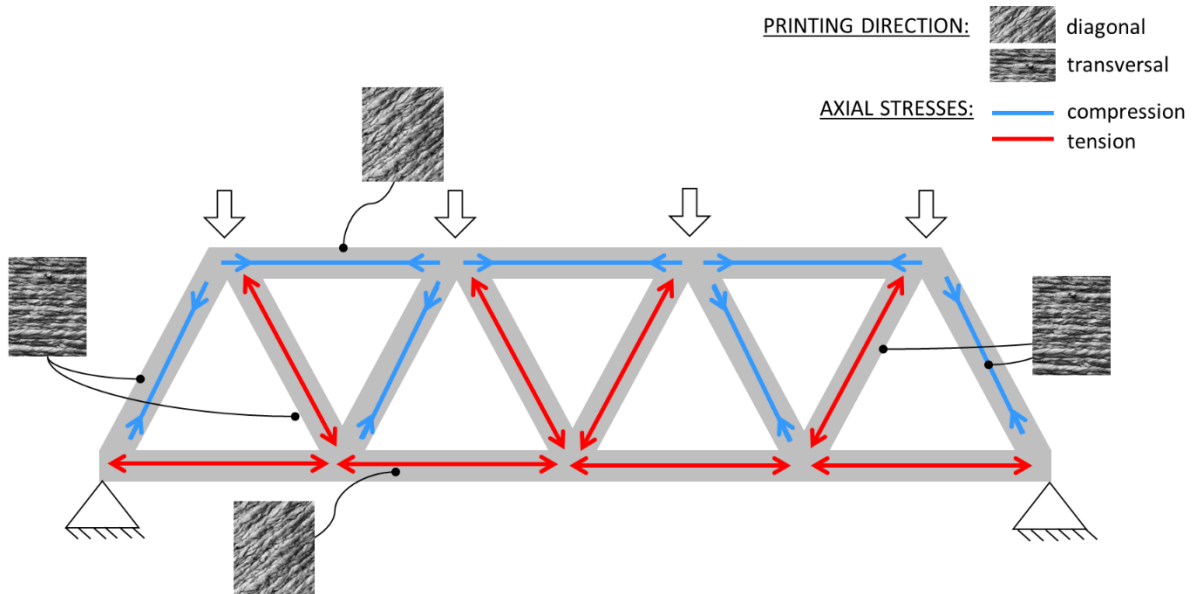


Figure 13: Graphical example of how to vary the printing directions in order to follow the orientation of highest axial stiffness in a WAAM planar truss system.

## 6. Conclusions

The study introduces an experimentally-validated orthotropic material model for Wire-and-Arc Additively Manufactured (WAAM) stainless steel on the basis of tensile and microstructural characterization.

The obtained results allow to draw the following concluding remarks:

- From the mechanical tests carried out on plates, a marked anisotropic behavior is registered for specimens cut along three main directions with respect to the printing deposition layers (T, L and D). In particular, the relationship found between Young's moduli and Poisson's ratios evaluated for specimens along L and T is such that symmetry of an orthotropic material model with principal axes L and T is satisfied.
- The microstructural investigations confirmed that grain growth is perpendicular to the printing deposition layers. In-depth analyses by means of XRD and EBSD evidenced the presence of preferential crystallographic orientations for specimens taken along T, L and D directions, clearly related to the elastic anisotropy of the fcc crystal structure of 304L stainless steel.
- From the elastic parameters evaluated through experiments, an orthotropic material model has been calibrated from the experimental results on four WAAM-produced stainless steel single-layer thick plates assuming that the symmetric axes of the model are coincident with the directions parallel and perpendicular to the printing layers (i.e. L and T, respectively). The Poisson's ratios calibrated to enforce symmetry of the compliance matrix of each lamina fit well the experimental results.
- The orthotropic model for WAAM stainless steel allows to predict the material elastic behavior along any printing orientation. In particular, the maximum value of Young's modulus was found for an inclination of  $42^\circ$  from the printing layers, having a value almost 50% larger than the traditionally manufactured one. Moreover, the variation of shear modulus values with respect to the relative orientation was estimated, with minimum value 50% lower than the traditionally manufactured one, while maximum value double than it.

These outcomes lead to a marked orthotropic behavior whose theoretical predictions in terms of orientations of maximum/minimum stiffness should be completely validated through additional experimental tests, including a detailed assessment of the inelastic behavior up to failure. A fully validated orthotropic material model can be then adopted to design optimized structural elements of minimum weight, through suitable orientations of the members relative to the required stiffness demand. The wide range of stiffness values (of the order of 2 for Young's modulus and 3.5 for shear

modulus) could be efficiently used to design deformation-driven solutions which are currently unexplored.

It should be finally noted that the specific remarks summarized in the previous bullets, although related to the WAAM-produced stainless steel plates fabricated with a unique set of parameters, can be considered of significant relevance since the investigated manufacturing process represents the current state-of-art for large-scale WAAM elements suitable for structural applications. In any case, future studies should be carried out to evaluate the influence of different process parameters in the mechanical and microstructural features and to extend the relevance of the proposed orthotropic model.

## Acknowledgements

The support of Dutch company MX3D held in Amsterdam is gratefully acknowledged for giving the additive-manufactured elements tested.

## References

- [1] K.S. Derekar, A review of wire arc additive manufacturing and advances in wire arc additive manufacturing of aluminium, *Mater. Sci. Technol.* (United Kingdom). 34 (2018) 895–916. <https://doi.org/10.1080/02670836.2018.1455012>.
- [2] T.A. Rodrigues, V. Duarte, R.M. Miranda, T.G. Santos, J.P. Oliveira, Current status and perspectives on wire and arc additive manufacturing (WAAM), *Materials* (Basel). 12 (2019). <https://doi.org/10.3390/ma12071121>.
- [3] C. Buchanan, L. Gardner, Metal 3D printing in construction: A review of methods, research, applications, opportunities and challenges, *Eng. Struct.* 180 (2019) 332–348. <https://doi.org/10.1016/j.engstruct.2018.11.045>.
- [4] A. Basak, S. Das, Epitaxy and Microstructure Evolution in Metal Additive Manufacturing, *Annu. Rev. Mater. Res.* 46 (2016) 125–149. <https://doi.org/10.1146/annurev-matsci-070115-031728>.
- [5] J.J. Lewandowski, M. Seifi, Metal Additive Manufacturing: A Review of Mechanical Properties, *Annu. Rev. Mater. Res.* 46 (2016) 151–186. <https://doi.org/10.1146/annurev-matsci-070115-032024>.
- [6] J. V. Gordon, C. V. Haden, H.F. Nied, R.P. Vinci, D.G. Harlow, Fatigue crack growth anisotropy, texture and residual stress in austenitic steel made by wire and arc additive manufacturing, *Mater. Sci. Eng. A.* 724 (2018) 431–438. <https://doi.org/10.1016/j.msea.2018.03.075>.
- [7] J. Wang, Z. Pan, Y. Wang, L. Wang, L. Su, D. Cuiuri, Y. Zhao, H. Li, Evolution of crystallographic orientation, precipitation, phase transformation and mechanical properties realized by enhancing deposition current for dual-wire arc additive manufactured Ni-rich NiTi alloy, *Addit. Manuf.* 34 (2020)

101240.

- [8] P. Jin, Y. Liu, Q. Sun, Evolution of crystallographic orientation, columnar to equiaxed transformation and mechanical properties realized by adding TiCps in wire and arc additive manufacturing 2219 aluminum alloy, *Addit. Manuf.* 39 (2021) 101878. <https://doi.org/https://doi.org/10.1016/j.addma.2021.101878>.
- [9] J. Ge, J. Lin, Y. Chen, Y. Lei, H. Fu, Characterization of wire arc additive manufacturing 2Cr13 part: Process stability, microstructural evolution, and tensile properties, *J. Alloys Compd.* 748 (2018) 911–921. <https://doi.org/10.1016/j.jallcom.2018.03.222>.
- [10] M. Rafieazad, M. Ghaffari, A. Vahedi Nemani, A. Nasiri, Microstructural evolution and mechanical properties of a low-carbon low-alloy steel produced by wire arc additive manufacturing, *Int. J. Adv. Manuf. Technol.* 105 (2019) 2121–2134. <https://doi.org/10.1007/s00170-019-04393-8>.
- [11] V. Chakkravarthy, S. Jerome, Printability of multiwalled SS 316L by wire arc additive manufacturing route with tunable texture, *Mater. Lett.* 260 (2020) 126981. <https://doi.org/https://doi.org/10.1016/j.matlet.2019.126981>.
- [12] M. Ghaffari, A. Vahedi Nemani, M. Rafieazad, A. Nasiri, Effect of Solidification Defects and HAZ Softening on the Anisotropic Mechanical Properties of a Wire Arc Additive-Manufactured Low-Carbon Low-Alloy Steel Part, *Jom.* 71 (2019) 4215–4224. <https://doi.org/10.1007/s11837-019-03773-5>.
- [13] P. Moore, A. Addison, M. Nowak-Coventry, Mechanical properties of wire plus arc additive manufactured steel and stainless steel structures, *Weld. World.* 63 (2019) 1521–1530. <https://doi.org/10.1007/s40194-019-00775-4>.
- [14] A.S. Yildiz, K. Davut, B. Koc, O. Yilmaz, Wire arc additive manufacturing of high-strength low alloy steels: study of process parameters and their influence on the bead geometry and mechanical characteristics, (2020).
- [15] L. Sun, F. Jiang, R. Huang, D. Yuan, C. Guo, J. Wang, Anisotropic mechanical properties and deformation behavior of low-carbon high-strength steel component fabricated by wire and arc additive manufacturing, *Mater. Sci. Eng. A.* 787 (2020) 139514. <https://doi.org/10.1016/j.msea.2020.139514>.
- [16] L. Ji, J. Lu, C. Liu, C. Jing, H. Fan, S. Ma, Microstructure and mechanical properties of 304L steel fabricated by arc additive manufacturing, *MATEC Web Conf.* 128 (2017). <https://doi.org/10.1051/mateconf/201712803006>.
- [17] P. Kyvelou, H. Slack, D.D. Mountanou, M.A. Wadee, T. Ben Britton, C. Buchanan, L. Gardner, Mechanical and microstructural testing of wire and arc additively manufactured sheet material, *Mater. Des.* (2020) 108675. <https://doi.org/10.1016/J.MATDES.2020.108675>.
- [18] V. Laghi, M. Palermo, G. Gasparini, V.A. Girelli, T. Trombetti, Geometrical characterization of Wire-and-Arc Additive Manufactured steel elements, *VBRI Press Adv. Mater. Lett.* 10 (2019) 695–699.
- [19] V. Laghi, M. Palermo, G. Gasparini, V.A. Girelli, T. Trombetti, Experimental results for structural



- design of Wire-and-Arc Additive Manufactured stainless steel members, *J. Constr. Steel Res.* 167 (2020). <https://doi.org/10.1016/j.jcsr.2019.105858>.
- [20] V. Laghi, M. Palermo, L. Tonelli, G. Gasparini, L. Ceschini, T. Trombetti, Tensile properties and microstructural features of 304L austenitic stainless steel produced by wire-and-arc additive manufacturing, *Int. J. Adv. Manuf. Technol.* (2020) 3693–3705. <https://doi.org/10.1007/s00170-019-04868-8>.
- [21] V. Laghi, M. Palermo, G. Gasparini, M. Veljkovic, T. Trombetti, Assessment of design mechanical parameters and partial safety factors for Wire-and-Arc Additive Manufactured stainless steel, *Eng. Struct.* 225 (2020) 111314. <https://doi.org/10.1016/j.engstruct.2020.111314>.
- [22] V. Laghi, M. Palermo, G. Gasparini, V.A. Girelli, T. Trombetti, On the influence of the geometrical irregularities in the mechanical response of Wire-and-Arc Additively Manufactured planar elements, *J. Constr. Steel Res.* 178 (2021) 106490. <https://doi.org/10.1016/j.jcsr.2020.106490>.
- [23] MX3D Webpage, (n.d.). [www.mx3d.com](http://www.mx3d.com).
- [24] DIN EN 10002-1:2001, Metallic materials - Tensile testing, *Met. Mater. - Tensile Test.* (2001) 54.
- [25] Metallic materials — Tensile testing — Part 1: Method of test at room temperature Matériaux métalliques — Essai de traction — Partie 1: Méthode d’essai à température ambiante COPYRIGHT PROTECTED DOCUMENT, Iso 6892-1. (2009). <http://files.instrument.com.cn/FilesCenter/20090913/200991371610112081.pdf>.
- [26] B. Strnadel, J. Brumek, The Size Effect in Tensile Test of Steels, (2013). <https://doi.org/10.1115/PVP2013-98162>.
- [27] A. Kohyama, K. Hamada, H. Matsui, Specimen size effects on tensile properties of neutron-irradiated steels, *J. Nucl. Mater.* 179–181 (1991) 417–420. [https://doi.org/10.1016/0022-3115\(91\)90113-L](https://doi.org/10.1016/0022-3115(91)90113-L).
- [28] ASTM International, E3 Preparation of Metallographic Specimens, *Annu. B. ASTM Stand.* 11 (2017) 1–17. <https://doi.org/10.1520/E0003-11R17.1>.
- [29] G.F. Vander Voort, G.M. Lucas, E.P. Manilova, Metallography and microstructures of stainless steels and maraging steels, *Mater. Park. OH ASM Int.* (2004) 670–700.
- [30] P. Saikia, A. Joseph, R. Rane, B.K. Saikia, S. Mukherjee, Role of substrate and deposition conditions on the texture evolution of titanium nitride thin film on bare and plasma-nitrided high-speed steel, *J. Theor. Appl. Phys.* 7 (2013) 66. <https://doi.org/10.1186/2251-7235-7-66>.
- [31] M. Liu, H. Liu, D. Wang, B. Liu, Y. Shi, F. Li, Y. Gong, L. Li, L. Li, W. Zhang, Effect of nanodiamond concentration and the current density of the electrolyte on the texture and mechanical properties of Ni/Nanodiamond composite coatings produced by electrodeposition, *Materials (Basel)*. 12 (2019). <https://doi.org/10.3390/ma12071105>.
- [32] V. Laghi, M. Palermo, G. Gasparini, V.A. Girelli, T. Trombetti, On the influence of the geometrical irregularities in the mechanical response of Wire-and-Arc Additively Manufactured planar elements, *J.*

Constr. Steel Res. (2020).

[33] A.H. Committee, ASM Handbook, Volume 1: Properties and Selection: Irons, Steels, and High-Performance Alloys, n.d.

[34] A.K. Kaw, Mechanics of composite materials, CRC press, 2005.

[35] L. Wang, J. Xue, Q. Wang, Correlation between arc mode, microstructure, and mechanical properties during wire arc additive manufacturing of 316L stainless steel, Mater. Sci. Eng. A. 751 (2019) 183–190. <https://doi.org/10.1016/j.msea.2019.02.078>.

[36] B. Hutchinson, Critical assessment 16: Anisotropy in metals, Mater. Sci. Technol. (United Kingdom). 31 (2015) 1393–1401. <https://doi.org/10.1179/1743284715Y.0000000118>.

[37] H.M. Ledbetter, Monocrystal-Polycrystal Elastic Constants of a Stainless Steel, Phys. Status Solidi. 85 (1984) 89–96. <https://doi.org/10.1002/pssa.2210850111>.

[38] H.M. Ledbetter, Predicted monocrystal elastic constants of 304-type stainless steel, Phys. B+C. 128 (1985) 1–4. [https://doi.org/https://doi.org/10.1016/0378-4363\(85\)90076-2](https://doi.org/https://doi.org/10.1016/0378-4363(85)90076-2).

[39] A. Taliercio, Introduzione alla meccanica dei solidi, Società Editrice Esculapio, 2020.

[40] G. Staab, Laminar composites, Butterworth-Heinemann, 2015.

[41] P. Vannucci, The Polar Formalism, in: Anisotropic Elast., Springer, 2018: pp. 131–244.

[42] E.V. Morozov, V.V. Vasiliev, Determination of the shear modulus of orthotropic materials from off-axis tension tests, Compos. Struct. 62 (2003) 379–382. <https://doi.org/10.1016/j.compstruct.2003.09.008>.

[43] M. Bruggi, V. Laghi, T. Trombetti, Simultaneous design of the topology and the build orientation of Wire-and-Arc Additively Manufactured structural elements, Comput. Struct. 242 (2021) 106370. <https://doi.org/10.1016/j.compstruc.2020.106370>.